
Numerical Simulation of the Hypersonic Flow Around Lifting Vehicles

Yehia Rizk, Denny Chaussee, and Joseph Steger

(NASA-TM-89444) NUMERICAL SIMULATION OF THE
HYPERSONIC FLOW AROUND LIFTING VEHICLES

N87-22116

(NASA) 28 p Avail: NTIS HC A03/MF A01

CSCL 20D

Unclas

G3/34 0066805

April 1987



National Aeronautics and
Space Administration

Numerical Simulation of the Hypersonic Flow Around Lifting Vehicles

Yehia Rizk, Sterling Federal Systems Inc., Palo Alto, California

Denny Chaussee, Joseph Steger, Ames Research Center, Moffett Field, California

April 1987



National Aeronautics and
Space Administration

Ames Research Center
Moffett Field, California 94035

NUMERICAL SIMULATION OF THE HYPERSONIC FLOW AROUND LIFTING VEHICLES

Yehia Rizk

Sterling Federal Systems Inc., Palo Alto, California, 94303.

Denny Chaussee and Joseph Steger

Nasa Ames Research Center, Moffett Field, California, 94035.

ABSTRACT

A method for solving the viscous hypersonic flow field around realistic configurations is presented. The numerical procedure for generating the required finite difference grid and the two-factored implicit flow solver are described. Results are presented for the shuttle orbiter and a generic wing-body configuration at hypersonic Mach numbers.

1. INTRODUCTION

With the continuous development of more powerful computers, computational fluid dynamics (CFD) has emerged as a viable tool in understanding complicated three-dimensional fluid dynamics phenomena in subsonic, transonic and supersonic flow regimes. Hence CFD is now being routinely applied to practical problems to supplement wind tunnel experimentation in the design process. The recent renewed international interest in hypersonic transport is partly attributed to the confidence in using CFD solely in design because of the impossibility of simulating the wide range of the actual hypersonic flight conditions in a wind tunnel. This of course necessitates the development of robust hypersonic CFD codes which are reliable for providing important quantities such as the aerodynamic stresses, heat transfer and inlet flow conditions to the engine.

In this paper we describe and apply a numerical technique which is capable of solving the hypersonic flow around three dimensional lifting configurations. In this technique, the computational grid is created using an efficient numerical hyperbolic grid generation procedure (Ref.[1]) and the equations of motion (represented by the Reynolds averaged Navier-Stokes equations) are integrated using the time-dependent factored procedure described in Ref.[2].

The present numerical procedure is used to compute the viscous flow around the shuttle orbiter at Mach number of 7.9 and angle of attack of 25 degrees and around a generic wing-body configuration at Mach number 25 and 5 degrees angle

of attack. In both cases the fluid was assumed to behave as a perfect gas. The calculations were performed on the CRAY-2 to allow the use of fine grids in order to resolve the details of the complicated flow field associated with the geometries under consideration.

In the following sections, we briefly describe the grid generation procedure, the flow simulation procedure, and the computed results.

2. GRID GENERATION PROCEDURE

In computational fluid dynamics, a three dimensional body fitted mesh is highly desired and can be generated numerically using the elliptic (Refs.[3,4]), hyperbolic(Refs.[1,5]), parabolic or hybrid (Refs.[6,7]) schemes. All these schemes involve solving a set of partial differential equations and they all possess the desirable feature of allowing the user to specify an arbitrary point distribution along the body surface.

In the present study, the hyperbolic scheme was chosen because it automatically creates a body normal grid which is important for viscous flow computations. Also, the hyperbolic grid generation method is efficient in terms of computer time and memory and the resulting grid can be made orthogonal or close to orthogonal everywhere by proper surface grid specification. The major drawback of the hyperbolic scheme is its inability to prescribe an exact location for the outer boundary. However, with a minor modification, the user can specify an approximate location for the outer boundary as will be discussed later. This limited control on the outer boundary shape suffices for a wide range of external flow problems.

The Hyperbolic grid is generated by solving for the cartesian coordinates x, y , and z , in terms of the generalized coordinates ξ, η , and ζ where, in general:

$$\xi = \xi(x, y, z)$$

$$\eta = \eta(x, y, z)$$

$$\zeta = \zeta(x, y, z)$$

here ξ is the streamwise coordinate, η is the circumferential coordinate and ζ is the outward coordinate.

A set of three equations are required to solve for the three unknowns x, y and z . Following Ref.[1], the first two equations are obtained by enforcing orthogonality relations between ξ and ζ lines and between η and ζ lines, whereas the third

equation is obtained from the cell volume specification. The following set of partial differential equations result:

$$\vec{r}_\xi \cdot \vec{r}_\zeta = 0 \quad (1a)$$

$$\vec{r}_\eta \cdot \vec{r}_\zeta = 0 \quad (1b)$$

$$\left| \frac{\partial(x, y, z)}{\partial(\xi, \eta, \zeta)} \right| = J^{-1} = \Delta V \quad (1c)$$

where \vec{r} is defined as $(x, y, z)^T$

The above nonlinear system of equations are locally linearized about the previous step which results in

$$A_l \delta_\xi(\vec{r}_{l+1} - \vec{r}_l) + B_l \delta_\eta(\vec{r}_{l+1} - \vec{r}_l) + C_l \nabla_\zeta \vec{r}_{l+1} = \vec{g}_{l+1} \quad (2)$$

where A_l, B_l and C_l are 3×3 coefficient matrices that are formed from the local linearization of Eq.(1). The vector \vec{g}_{l+1} contains the user specified cell volumes

$$\vec{g}_{l+1} = \begin{pmatrix} 0 \\ 0 \\ \Delta V_{l+1} \end{pmatrix}$$

In Eq.(2), δ is the central difference operator used in ξ and η directions whereas ∇ is the backward differencing used in ζ direction. Using approximate factorization, Eq.(2), is reduced to

$$\mathcal{L}_\eta \mathcal{L}_\xi(\vec{r}_{l+1} - \vec{r}_l) = C_l^{-1} \vec{g}_{l+1} \quad (3)$$

where \mathcal{L}_η and \mathcal{L}_ξ are block tridiagonal matrices given by:

$$\mathcal{L}_\eta = (I + C_l^{-1} B_l \delta_\eta)$$

$$\mathcal{L}_\xi = (I + C_l^{-1} A_l \delta_\xi)$$

Therefore, the vector \vec{r}_{l+1} is obtained by solving the following sequence:

$$\mathcal{L}_\eta \vec{g}_{l+1}^* = C_l^{-1} \vec{g}_{l+1}$$

$$\mathcal{L}_\xi \nabla_\zeta \vec{r}_{l+1} = \vec{g}_{l+1}^*$$

$$\vec{r}_{l+1} = \vec{r}_l + \nabla_\zeta \vec{r}_{l+1}$$

Starting from the body surface, the mesh is obtained by marching outward using Eq.(3). In order to improve stability, numerical dissipation terms are added in the

ξ and η directions. The dissipation consists of second-order implicit and fourth-order explicit terms which are scaled to the local mesh spacing (Ref.[1]). Additional optional implicit smoothing(Ref.[8]) is used for complicated body shapes to prevent grid line intersection near highly concave sections.

Depending on the boundary conditions specified at the ξ direction, the user can create "C-O" (Fig. 1a) or "H-O" (Fig. 1b) meshes suitable for supersonic external flow problems. The boundary condition procedure developed in Ref.[1] is employed at $\xi = 0$ and $\xi = \xi_{max}$. This procedure takes advantage of the fact that the eigenvalues of either $C_l^{-1}A$ or $C_l^{-1}B$ are of the form $(\sigma, 0, -\sigma)$ where σ is real. The zero eigen value permits the specification of a combination of the dependent variables(e.g. $z = f(x, y)$) or the use of one sided differencing at the boundary. Hence, either one of the following two stable boundary procedure can be used. The first is to specify one combination of the dependent variables and use one sided differencing for the two remaining governing equations at the boundary. This approach is used at a boundary surface (e.g. $\xi = \xi_{max}$ in Figs. 1a, 1b) The second procedure is to specify two combinations of the dependent variables and use one sided differencing for a third governing equation at the boundary. this approach is used at an axis (e.g. $\xi = 0$ in Fig. 1a). In both cases, periodicity is assumed in the η direction.

The surface grid can be arbitrarily specified by the user. For relatively simple body shapes, the user can generate an orthogonal grid along the body surface. This process assures that the resulting grid will be nearly orthogonal in all directions. For complicated configurations, however, the surface grid is generated along cross sections of constant axial distance. Depending on the body shape, the ξ and η lines can be far from being orthogonal. However, this does not introduce any inconsistency because the orthogonality between the ξ and η is not enforced in the grid generation procedure. Experience has shown that the overall quality of the mesh is dependent upon the quality of the surface grid. Therefore, the user should pay extra attention in defining the surface grid to ensure a well behaved grid everywhere.

Since the grid is obtained by marching outward from the body, an exact location for the outer boundary can not be prescribed. Nevertheless, an approximate location for the outer boundary can be specified through proper selection of the cell volumes used in Eq. (1c). The cell volumes are defined by connecting straight lines between the surface boundary and the desired outer boundary shape. A prescribed clustering is then used to define the points along each ζ line. These cell volumes are then used in Eq.(1c) for the marching process. The resulting outer boundary will be close to the desired boundary. If a more exact outer boundary shape is needed, the computed grid points can be reclustered in the ζ direction to allow that. This is accomplished by calculating the intersection of the computed ζ lines with the desired boundary. The grid points are then obtained by redistributing points between the body and

the calculated intersection points along each line using the prescribed clustering. Although, the grid remains body normal, a significant amount of mesh skewness can be introduced especially if the desired outer boundary is relatively close to the body surface. This can be remedied by adding an extra global marching pass to improve the quality of the grid. This is done by computing new cell volumes at the end of the first global marching step and using that as the specified cell volume for the second global step.

3. FLOW SIMULATION PROCEDURE

Although in the current study we are dealing with predominantly supersonic flows, some regions of the flow field may contain pockets of embedded subsonic flow and/or axial separation. In such regions, the flow equations are elliptic, precluding the use of the more efficient space-marching techniques such as the parabolized Navier-Stokes (PNS) codes (e.g. Ref. [9]). Instead, a time-dependent procedure (F3D) is used to find the steady-state solution of the three-dimensional conservation-law form of the Reynolds-averaged Navier-Stokes equations.

3.1 Numerical Procedure

The unsteady Navier-Stokes equations with the thin-layer approximation in a strong conservative form, can be written as:

$$\hat{Q}_t + \hat{E}_\xi + \hat{F}_\eta + \hat{G}_\zeta = Re^{-1} \hat{S}_\zeta \quad (4)$$

where \hat{Q} is the dependent variables vector, \hat{E} , \hat{F} and \hat{G} are the inviscid-flux vectors, and the \hat{S} is contribution from the viscous terms. These vectors are given in Ref.[2].

A first or second order upwind differencing is used in ξ (streamwise) direction while a second order central differencing is used in η (meridional) and ζ (normal) directions. The implicit non-iterative two-factored scheme developed in Ref.[2] is used to solve Eq.(4). In this scheme, the flow variables at time step $n + 1$ are obtained from :

$$\mathcal{L}^+ \mathcal{L}^- (\hat{Q}^{n+1} - \hat{Q}^n) = -\Delta t (\delta_\xi^b (\hat{E}^+)^n + \delta_\xi^f (\hat{E}^-)^n + \delta_\eta^c \hat{F}^n + \delta_\zeta^c \hat{G}^n - Re^{-1} \bar{\delta}_\zeta \hat{S}^n) \quad (5)$$

where, δ^c is the central operator, δ^b is the backward operator, δ^f is the forward operator and $\bar{\delta}$ is the midpoint central operator. In Eq.(5), \mathcal{L}^+ is a lower block triangular matrix and \mathcal{L}^- is an upper block triangular matrix and they are given by:

$$\mathcal{L}^+ = (I + h\Delta t \delta_\xi^b \hat{A}^+ + \delta_\zeta^c \hat{C} - Re^{-1} \bar{\delta}_\zeta (J^{-1} \hat{M} J))$$

$$\mathcal{L}^- = (I + h\Delta t \delta_\xi^f \hat{A}^- + \delta_\eta^c \hat{B})$$

where the 5×5 matrices $\hat{A}^\pm, \hat{B}, \hat{C}$ and \hat{M} are the flux Jacobians of the fluxes $\hat{E}^\pm, \hat{F}, \hat{G}$ and \hat{S} respectively.

Equation (5) is solved by a sequence of two one-dimensional like inversions. In practice, smoothing terms are added in the η and ζ directions where central spatial differencing is used. The smoothing consists of second order implicit terms and combination of second and fourth order explicit terms. Also, free stream is subtracted as a base solution to reduce the numerical differencing error.

In the above formulation, upwind differencing is used in the streamwise direction. In hypersonic flows, the bow shock is typically more aligned with ζ lines than with the ξ lines especially near the nose section where the bow shock is the strongest. Therefore, it would be more advantageous to use upwind differencing in the ζ direction and central differencing in the ξ and η directions. Without making significant changes to the code, upwind differencing can be utilized in the outward direction by simply interchanging ξ with ζ and neglecting the implicit portion of the viscous terms in Eq.(5) resulting in:

$$\mathcal{L}^+ \mathcal{L}^-(\hat{Q}^{n+1} - \hat{Q}^n) = -\Delta t(\delta_\zeta^b(\hat{G}^+)^n + \delta_\zeta^f(\hat{G}^-)^n + \delta_\eta^c \hat{F}^n + \delta_\xi^c \hat{E}^n - Re^{-1} \delta_\zeta \hat{S}^n) \quad (6)$$

where,

$$\mathcal{L}^+ = (I + h\Delta t \delta_\zeta^b \hat{C}^+ + \delta_\xi^c \hat{A})$$

$$\mathcal{L}^- = (I + h\Delta t \delta_\zeta^f \hat{C}^- + \delta_\eta^c \hat{B})$$

Here \hat{C}^\pm is the flux jacobian of \hat{G}^\pm . It must be noted that, while upwind differencing is used for the inviscid flux in the ζ direction, the viscous flux on the right hand side of Eq.(6) is still centrally differenced using the midpoint operator.

The above alternative formulation produces sharper bow shocks as will be shown later. Moreover, by interchanging the algorithm this way, the streamwise axis singularity(at which the grid transformation Jacobian is infinite)is tied to central differencing rather than the most sensitive upwind differencing. The obvious drawback is that the viscous terms are treated explicitly. This proved to reduce the maximum allowable time step increment resulting in slower convergence rates. The possibility of modifying the code in order to retain the implicit viscous terms in Eq.(6) will be addressed in a forthcoming report.

The normal flux split formulation is implemented into the code as an option. An input control parameter activates the calls to the appropriate boundary conditions subroutine. In order to compare the two formulations, the inviscid flow around the shuttle nose at Mach number of ≈ 7.9 and 25 degrees angle of attack was selected as a test case. The grid in the pitch plane of symmetry is shown in Fig. 2. Figures

3 and 4 show the computed steady state mach number contours in the pitch plane of symmetry obtained using streamwise flux split (Eq.(5)) and normal flux split (Eq.(6)), respectively. It is clearly seen that the normal flux split yields a much sharper bow shock definition near the nose and in the windward region where the shock is roughly aligned with ζ =constant surfaces. However, both the streamwise and normal flux split result in shock smearing in the downstream portion of the leeside. This is because the bow shock there is no longer aligned with either the ζ or ξ surfaces as could be seen from the grid in Fig. 2. It is worth noting that, with the normal flux split, a simple grid adaptation where the grid points are allowed to move on the ζ lines can solve this problem. In general, a formulation in which flux splitting is utilized in both the streamwise and normal directions may be more suitable for general hypersonic flow problems.

3.2 Boundary Conditions

At $\zeta = 0$ (body surface), the viscous no-slip condition is imposed. The normal momentum equation is used to compute the surface pressure. In addition, either an adiabatic wall condition or a prescribed wall temperature are specified. At $\zeta = \zeta_{max}$ (outer boundary), the bow shock can either be fitted or captured. In the bow-shock-capturing calculations, the boundary values are fixed at its free stream values. With the bow shock fitted, its location as well as the flow variables behind it are determined from the shock fitting procedure of Ref.[10]. The shock is allowed to move along the curved ζ lines. The original clustering is maintained by redistributing points along ζ lines after each time step to adjust for the bow shock movement.

In the present study only cases with bilateral symmetry are considered, and the boundary conditions in the meridional direction η enforces symmetry conditions at the $\eta = 0$ (leeward) and $\eta = \eta_{max}$ (windward) planes. The symmetry is imposed through the use of reflection points on the opposite sides of the leeward and windward planes.

At $\xi = 0$, either axis ("C-O" mesh) or inflow ("H-O" mesh) boundary conditions are imposed. At the axis the boundary conditions are obtained by extrapolating and then averaging the flow variables from the surrounding points. When upwind differencing is used in the streamwise direction, the flow variables at the first set of grid points away from the axis is obtained by interpolation to avoid integrating the equations of motion at these points. This interpolation step is not needed when central differencing is used in the streamwise direction. At the inflow boundary, all the flow variables are specified. At $\xi = \xi_{max}$ (outflow boundary) an extrapolation formula consistent with supersonic outflow is used.

All the boundary conditions are implemented explicitly in the code. While the use of explicit boundary conditions with an implicit scheme does cause some degradation of the convergence rates, the use of explicit boundary conditions allows the user to

treat different flow problems by merely changing the boundary conditions routines without changing the rest of the code.

4. RESULTS

The current grid generation and flow solution procedures have been used to simulate the hypersonic flow field around the shuttle orbiter and a generic wing-body configuration.

4.1 Shuttle Orbiter

Figure 5a shows an overall view of the mesh generated for the orbiter while Fig. 5b shows the details of the grid near the body surface. The three dimensional mesh is displayed by showing the surface grid ($\zeta = 0$), the grid in the plane of symmetry ($\eta = 0$ and $\eta = \eta_{max}$) and the grid at the exit plane ($\xi = \xi_{max}$). It is seen that the grid is well behaved and is body normal. In generating the mesh, an estimate for the bow shock location was made and the appropriate values for the cell volume were chosen to result in an outer boundary location suitable for shock capturing computations. The boundary procedure corresponding to Fig. 1a ("C-O" mesh) is used where the two relations $y = y(x)$ and $z = z(x)$ are employed at the axis. At the outflow boundary the relation $x = constant$ is employed. The value of the constant is determined from the surface grid. The grid is compromised of 54 points along the body, 61 points in the cross section and 45 points in the outward direction.

The flow conditions are $M_\infty = 7.9$ and $\alpha = 25$ degrees, and a constant wall temperature of 540 degrees. The Reynolds number (based on the orbiter total length) is 1.46×10^6 . The flow was assumed to be laminar. These flow conditions correspond to the wind tunnel experimental data of Ref. [11]. The calculations were performed using the streamwise flux split option. The result of the computations in the region where the wing shock interacts with the bow shock are shown in Figs. 6 and 7. Figure 6 shows the pressure contours at a typical cross section. The pressure and mach number contours in a $\eta = constant$ plane passing by the wing tip are shown in Fig. 7. The general features of the flow field near the surface is indicated in Fig. 8 which depicts the simulated oilflow pattern. Lines of cross flow separation are clearly visible on the upper wing and on the top part of the orbiter. Also, a line of axial flow separation is observed on the top surface. Fig. 9 show the variation of the surface pressure along the windward plane of symmetry and in a cross plane at $x/l = .796$. The experimental data at $x/l = .8$ is also shown, and it seen that there is a good agreement between the computed results and the data. The steady-state computations required about 7 MW of core memory and took about 8 hours of CRAY 2 time.

4.2 Generic Wing-Body Geometry

The flow about a generic wing body configuration was also computed. The flow conditions for this case are $M_\infty = 25$, $\alpha = 5$ degrees, and a constant wall temperature of 3000 degrees. A specific heat ratio of 1.2 was chosen to simulate the real gas effects at high freestream Mach number.

In order to facilitate the solution at this high Mach number, a segmentation procedure(Ref.[12]) in which the flow field is divided into two regions is used. The boundary between the two adjacent regions is carefully located beyond the rounded nose where the outer inviscid flow is supersonic and the boundary layer is attached. This ensures the absence of any upstream influence between the two regions. This division enables the use of shock fitting in the nose region where the shock is strongest, while shock capturing is used in the downstream section. The use of shock capturing in the second segment avoids the tedious process associated with guessing the initial bow shock shape for the shock fitting procedure.

The grid in the second segment was first created with the outer boundary located far away from the body. Then, the local bow shock slope at the end of first segment was used as guide for determining a more appropriate location for the outer boundary. The grid points were then redistributed in the ζ direction to reflect this new location as explained earlier. The boundary procedure corresponding to Fig. 1b ("H-O" mesh) is used where the relation $x = \text{constant}$ are employed at the inflow and the outflow boundaries. The surface and resulting computational grid (at the symmetry plane and exit plane) are shown in Fig. 10. The grid consisted of 45 points in the streamwise direction, 92 points in the meridional direction and only 26 points in the outward direction. It is seen that the grid is smooth and body normal everywhere except at $\xi = \xi_{max}$ where one of the orthogonality equations was replaced by the relationship $x = \text{constant}$ to ensure stable marching.

The computation was first performed with the original flux split formulation until steady state was reached. Then, the normal flux split option was activated to produce a better definition for the bow shock. The implicit viscous terms on the left hand side of Eq.(5) were neglected as mentioned before. This forced a reduction in the time step by an order of magnitude thus slowing down the convergence considerably. Figure 11 show the Mach number in a cross plane near the end of the vehicle. The pressure contours on the body surface are shown in Fig. 12. It is seen that there is a pressure rise near the nose and near the wing tip.

CONCLUDING REMARKS

The hyperbolic grid generation scheme allows the generation of a three dimensional body normal mesh suitable for viscous flow computations. The limited outer-boundary control is suitable for hypersonic applications. A method for solving the

viscous hypersonic flow field around realistic configurations on the CRAY2 computer was presented. Flux splitting was used in the streamwise and normal directions. The normal flux splitting results in a sharper bow shock and avoids the axis singularity problem but requires more iterations because of the explicit treatment of the viscous terms.

REFERENCES

1. Steger, J.L. and Rizk, Y.M., "Generation of Three Dimensional Body Fitted Coordinates Using Hyperbolic Partial Differential Equations.", NASA TM 86753, June, 1985.
2. Ying, S. and Steger, J. and Schiff, L. and Baganoff, D. "Numerical Simulation of Unsteady, Viscous, High Angle of Attack Flows Using a Partially Flux Split Algorithm.", AIAA Paper no. 86-2179.
3. Thompson, J.F., Proceedings of a Symposium on the Numerical Generation of Curvilinear Coordinate Systems and Their Use in the Numerical Solution of Partial Differential Equations. 1982, Nashville, Tennessee.
4. Sorenson, R. , "Elliptic Generation of Composite Three-Dimensional Grids about Realistic Aircraft.", NASA TM 88240, March, 1986.
5. Rizk, Y., Steger, J. and Chaussee, D., "Use of Hyperbolic Grid Generation Scheme in Simulating Supersonic Viscous Flow About Three Dimensional Winged Configurations.", International Symposium on Computational Fluid Dynamics. Tokyo, Japan, Sep. 9-12, 1985.
6. Edwards, T., "A Three Dimensional Grid Generation Using a Parabolic Partial Differential Equations.", AIAA Paper No. 85-0485, Reno, Nevada, Jan. 1985.
7. Nakamura, S. and Suzuki, M., "Noniterative Three Dimensional Grid Generation Using a Parabolic Hyperbolic Hybrid Scheme.", AIAA Paper No. 87-0227, Reno, Nevada, Jan., 1987.
8. Kinsey, D.W., and Barth, T.J., "Description of a Hyperbolic Grid Generation Procedure for Arbitrary Two-Dimensional Bodies.", AFWAL Technical Memorandum No. 84-191-FIMM (July, 1984)
9. Schiff, L.B., and Steger, J.L., "Numerical Simulation of Steady Supersonic Viscous Flow.", AIAA Journal, Vol.18, Dec. 1980., pp 1421-1430.
10. Kutler, P., Pedelty, J.A., and Pulliam, T.H., "Supersonic Flow Over Three-dimensional Ablated Nosed Tips Using Implicit Numerical Procedure.", AIAA Paper No. 80-0063, Pasadena, Calif., Jan., 1980.

11. Herrera, B. J., "Results of a Flowfield Survey Conducted Using The 0.0175 Scale Orbiter Model 29-0 in AEDC VKF Tunnel B During Test OH52" NASA CR-147, 637, Sep., 1976.

12. Rizk, Y.M., and Ben-shmuel, S., "Computation of the Viscous Flow Around the Shuttle Orbiter at Low Supersonic Speeds." AIAA Paper 85-0168, Reno, Nevada, Jan., 1985.

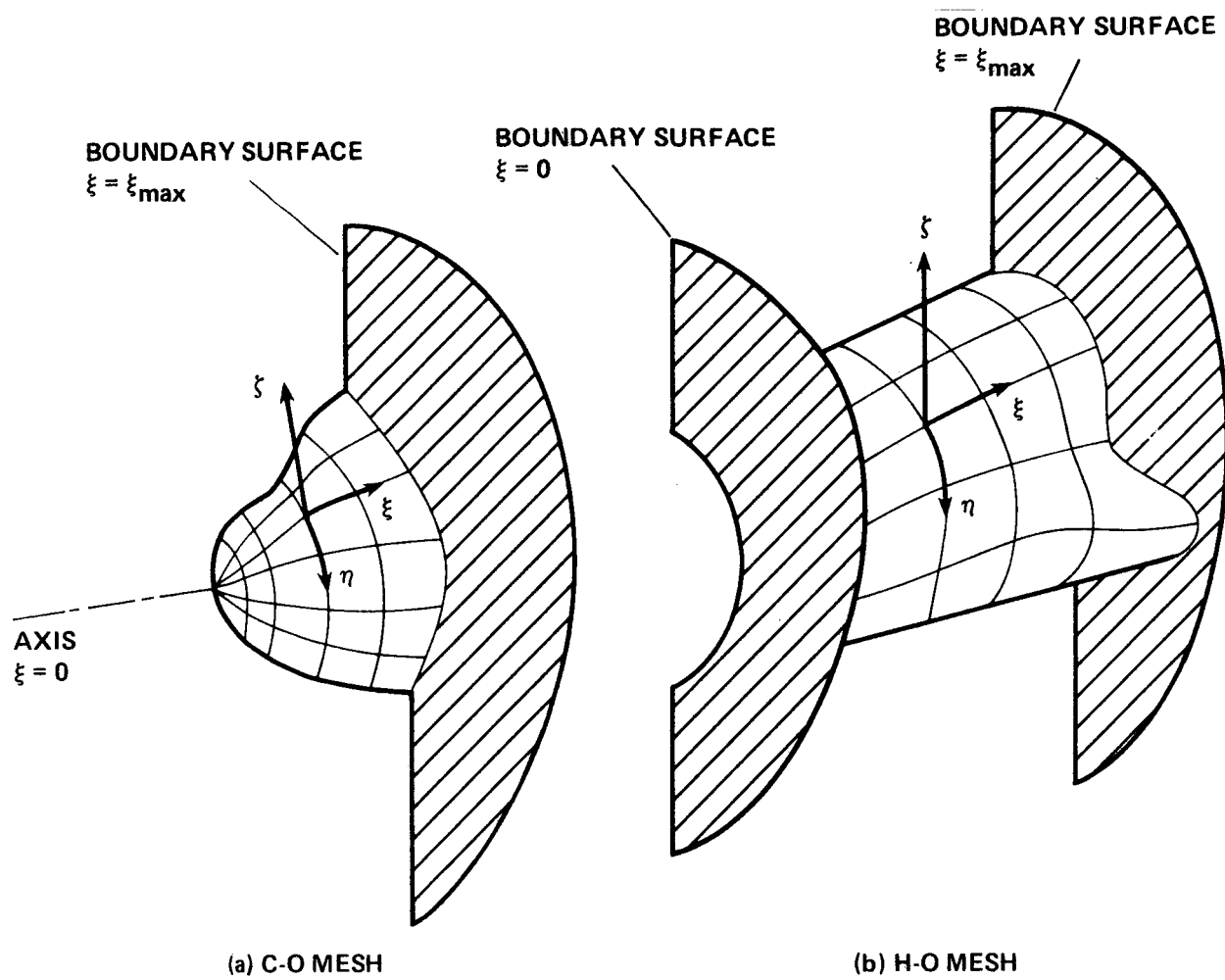


Figure 1. Mesh topologies for hypersonic flow computations.

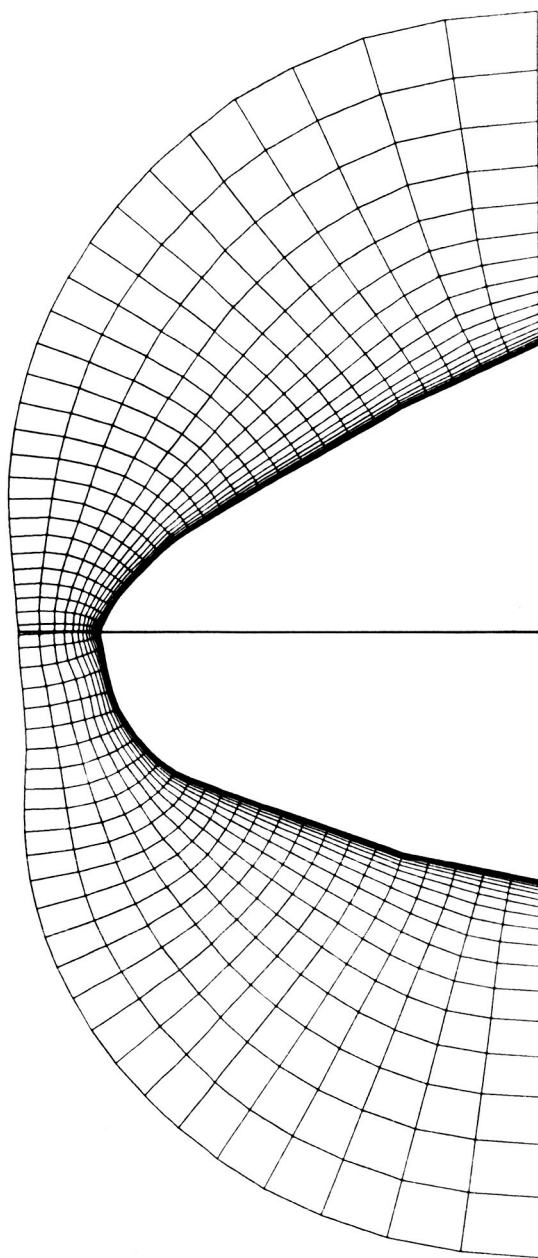


Figure 2. Computational grid around the shuttle nose.

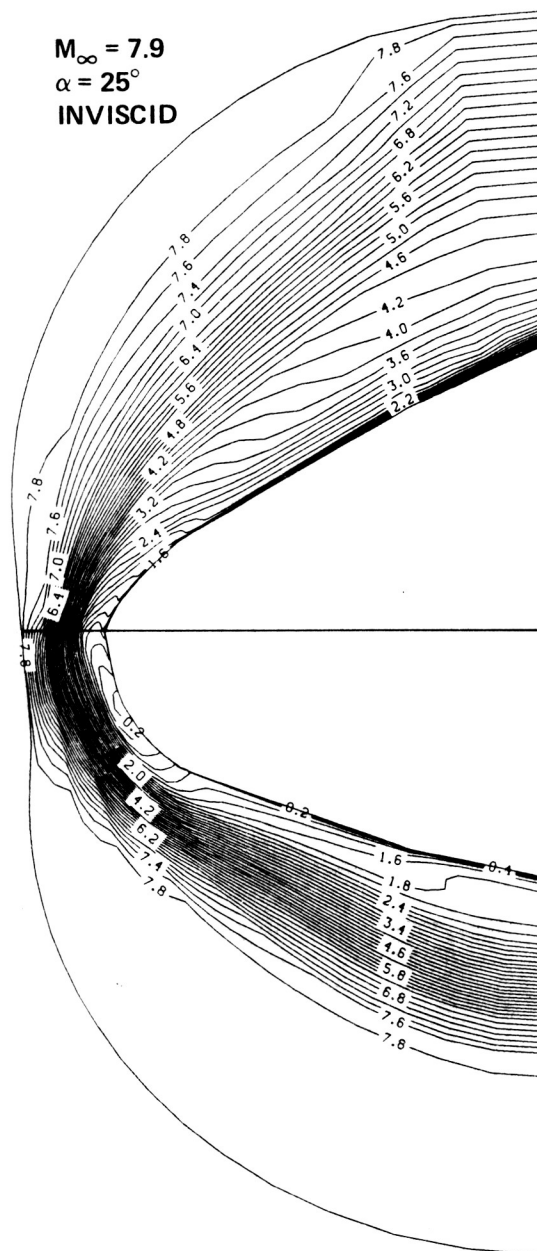


Figure 3. Mach number contours computed using streamwise flux splitting.

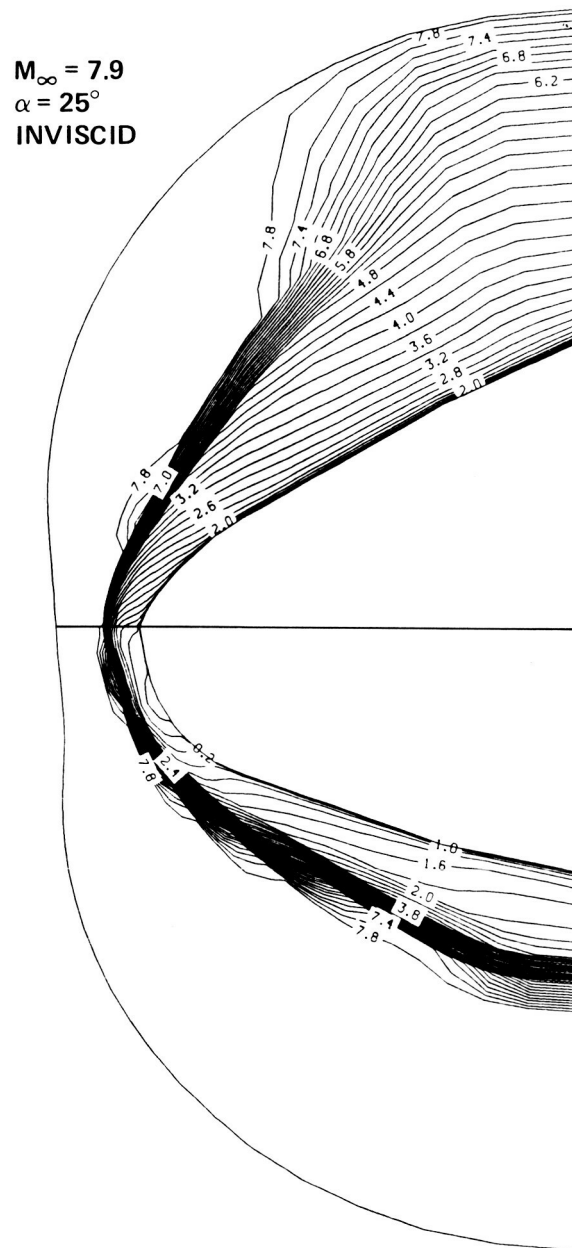


Figure 4. Mach number contours computed using normal flux splitting.

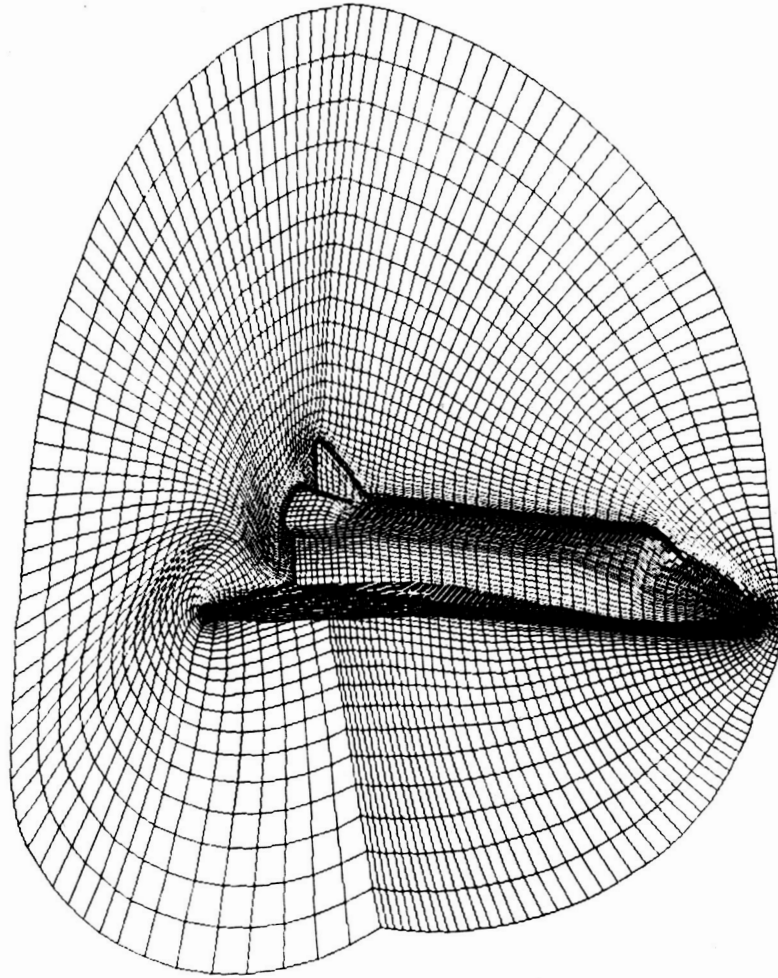


Figure 5a. Overall view of the computational grid for the orbiter.

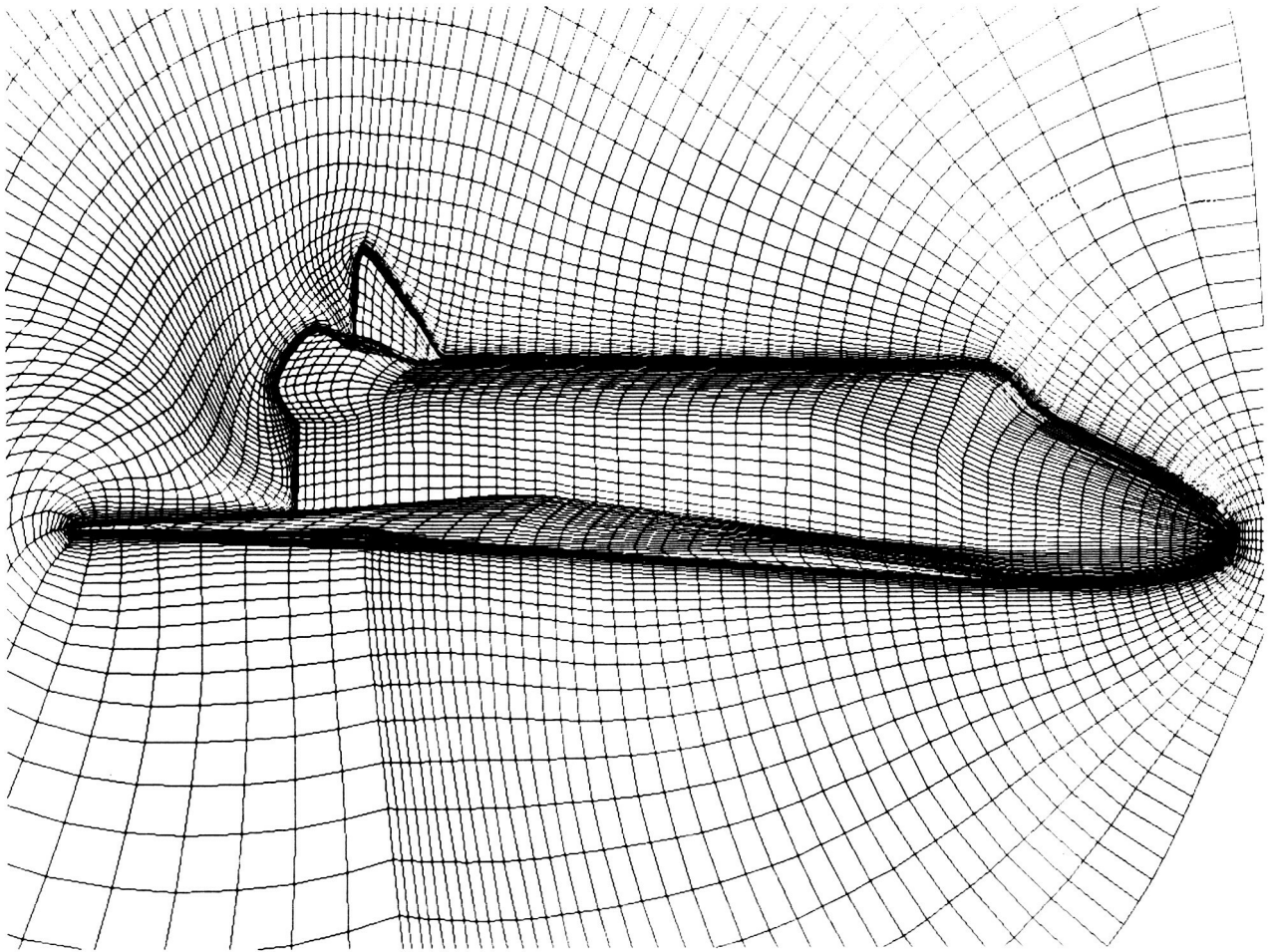


Figure 5b. Details of the computational grid near the orbiter surface.

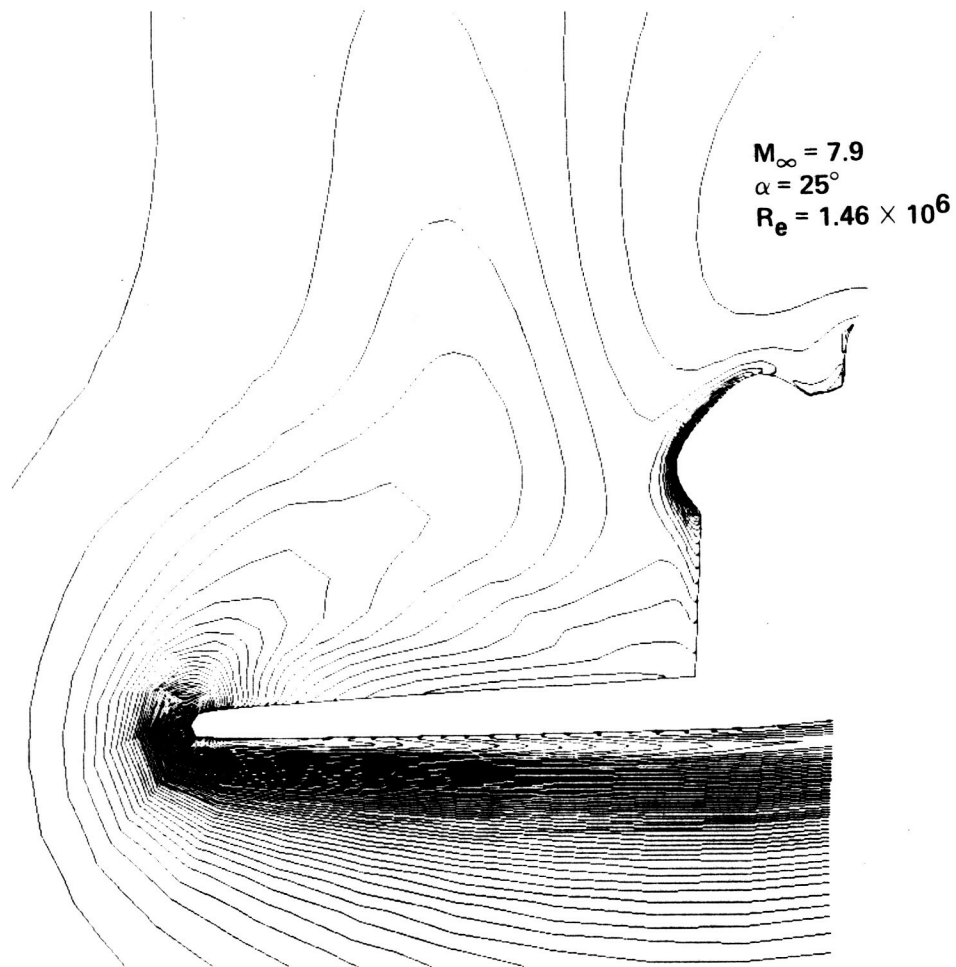


Figure 6. Pressure contours in a ξ constant plane near the end of the orbiter.

ORDERED LIST OF
OF POOR QUALITY

$M_\infty = 7.9$
 $\alpha = 25^\circ$
 $Re = 1.46 \times 10^6$

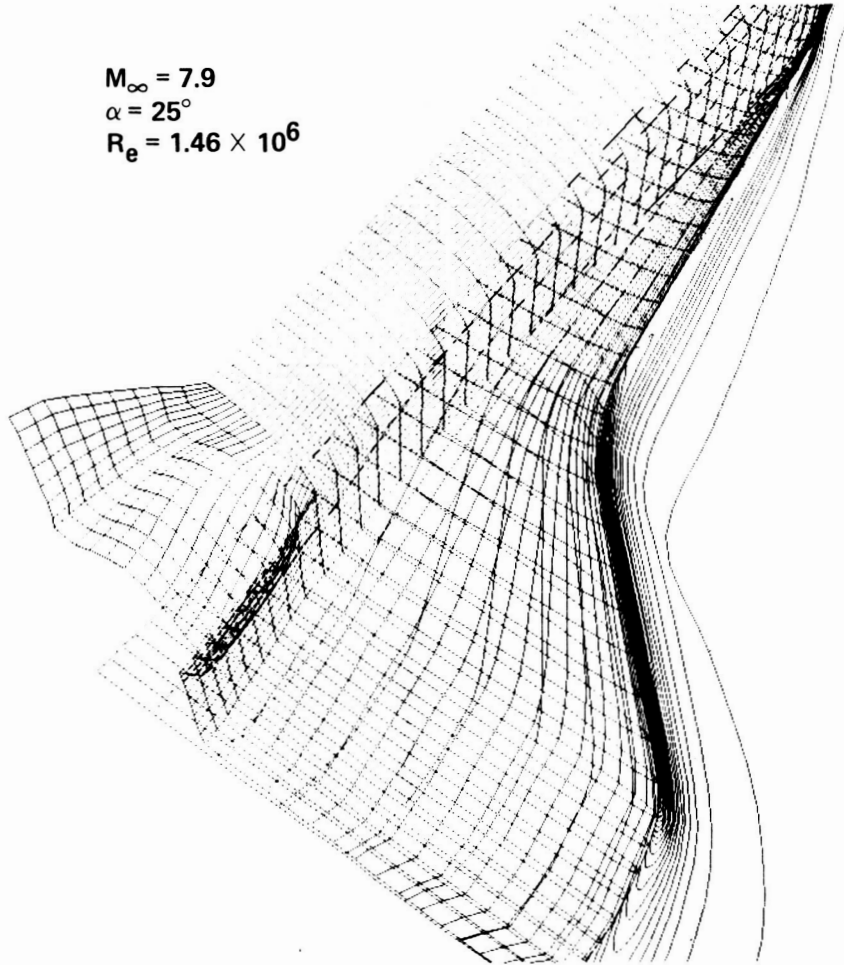


Figure 7a. Pressure contours in a η plane near the wing tip.

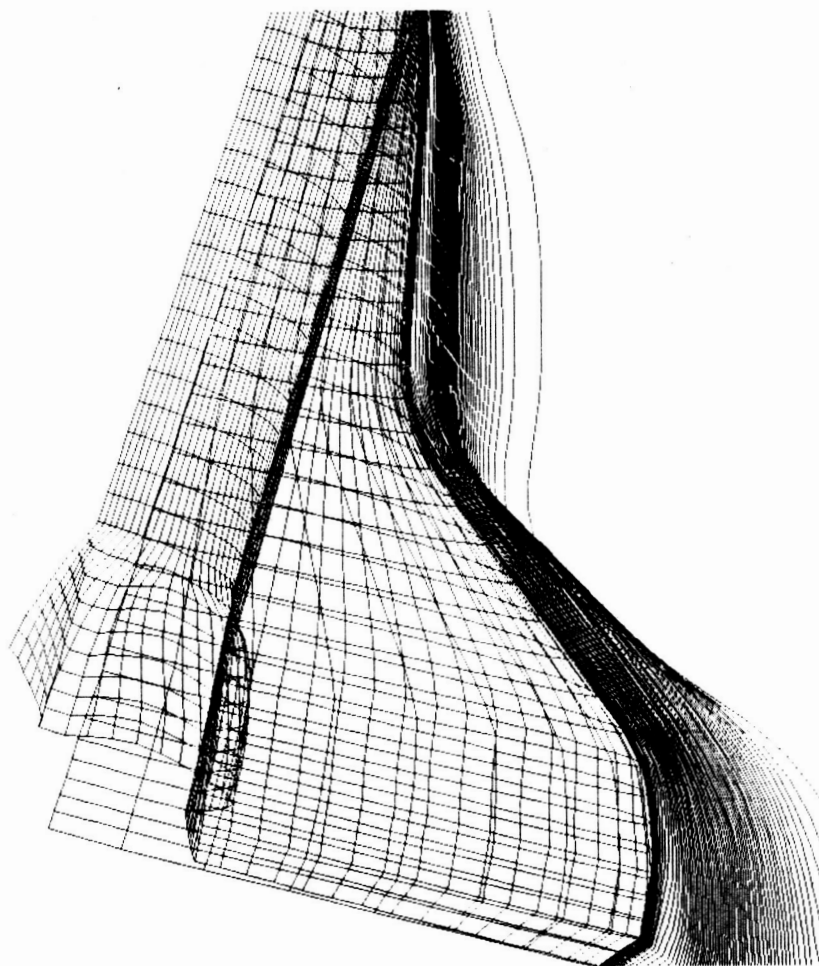


Figure 7b. Mach number contours in a η plane near the wing tip.

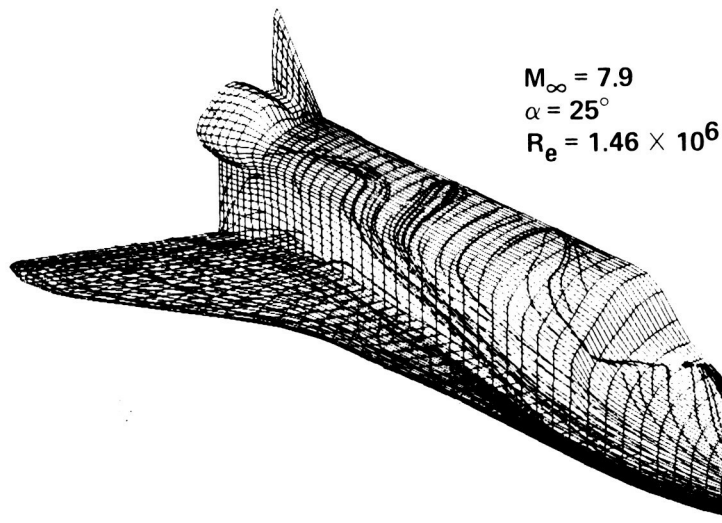


Figure 8. Computed limiting streamlines on the orbiter surface.

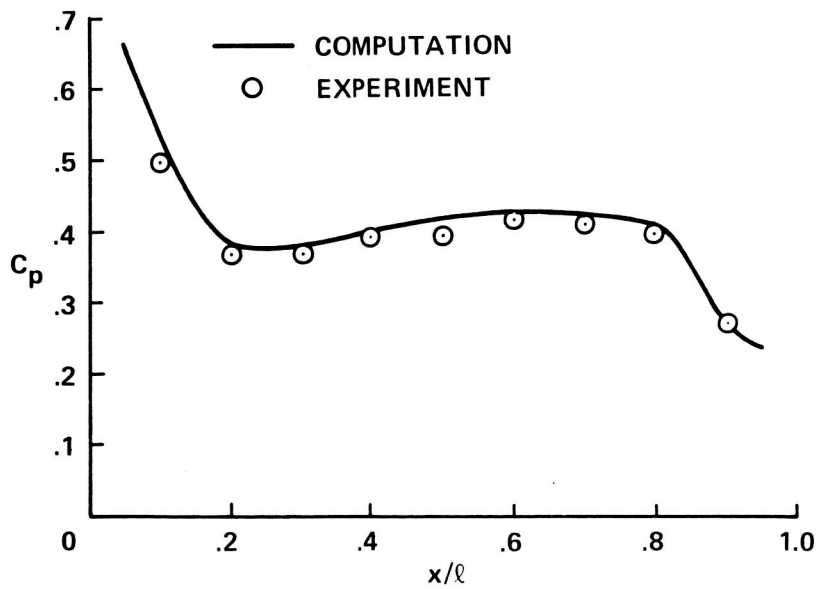


Figure 9a. Comparison between the computed pressure and the experimental data on the windward side.

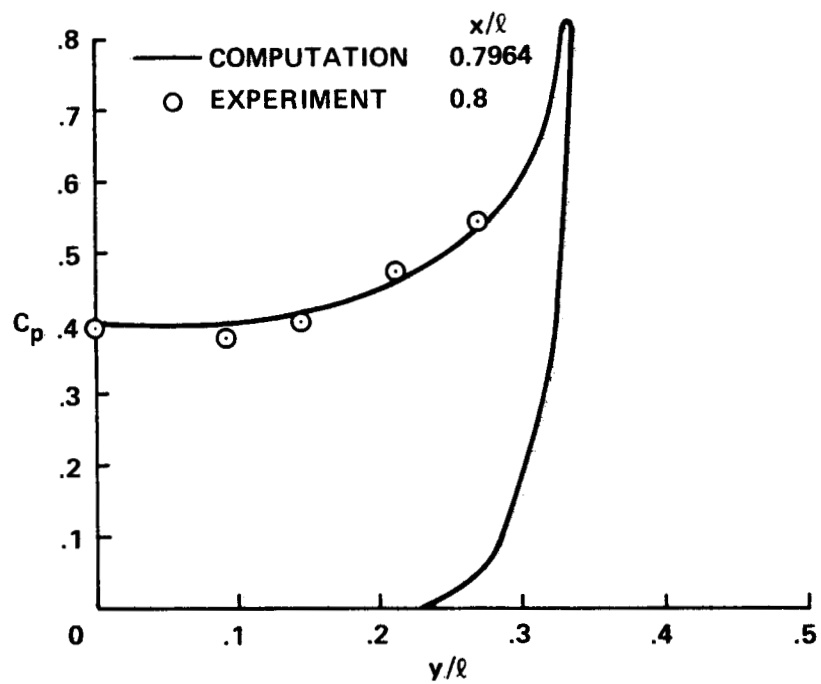


Figure 9b. Comparison between the computed pressure and the experimental data at $x/l = 0.8$.

ORIGINAL PAGE IS
OF POOR QUALITY

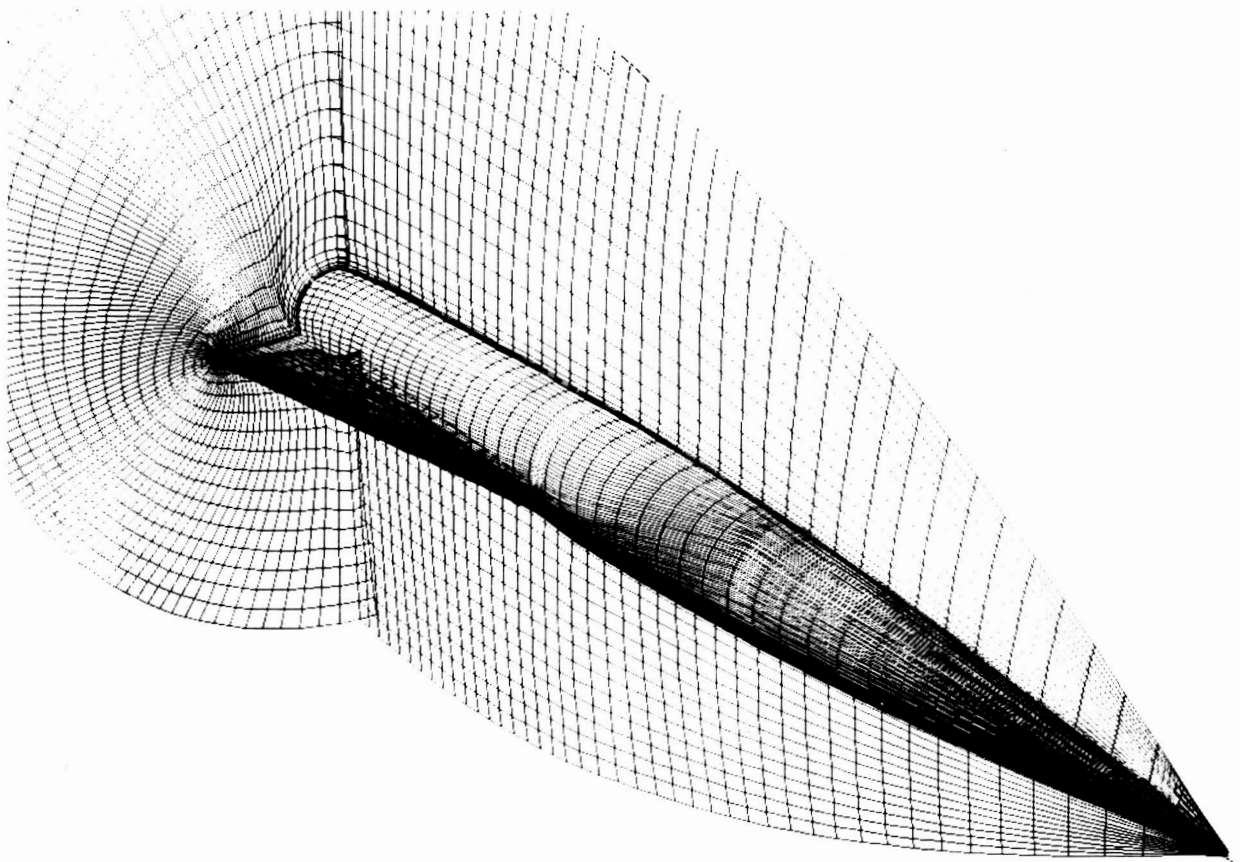


Figure 10. Computational grid for a generic wing body configuration.

ORIGINAL PAGE IS
OF POOR QUALITY

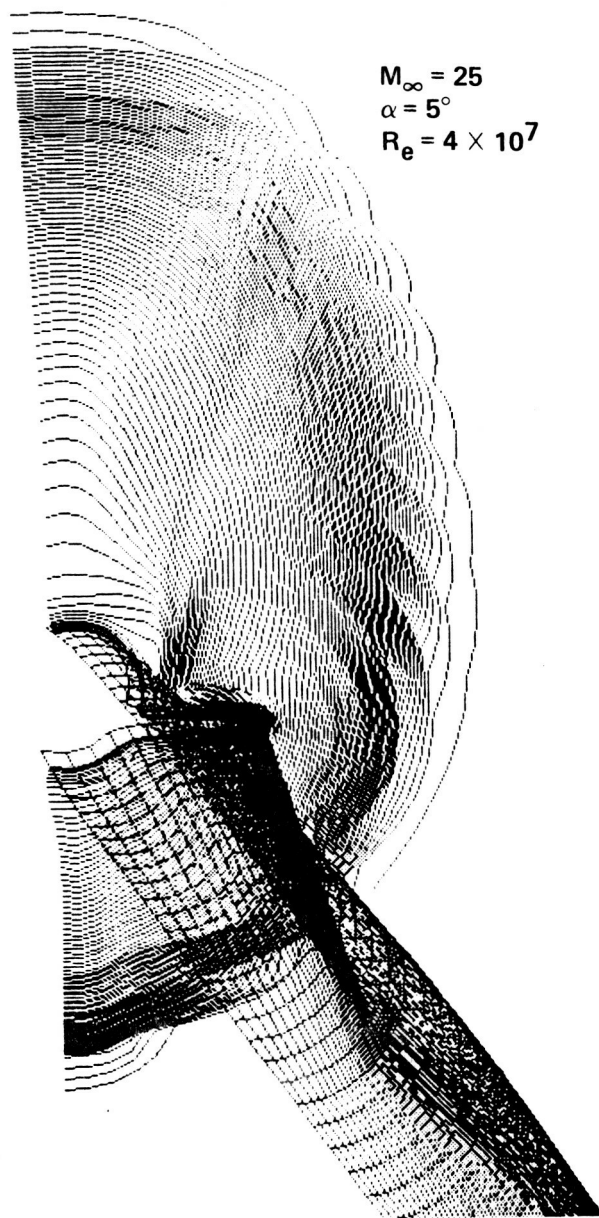


Figure 11. Mach number contours in a ξ constant plane near the end of the vehicle.

ORIGINAL PAGE IS
OF POOR QUALITY

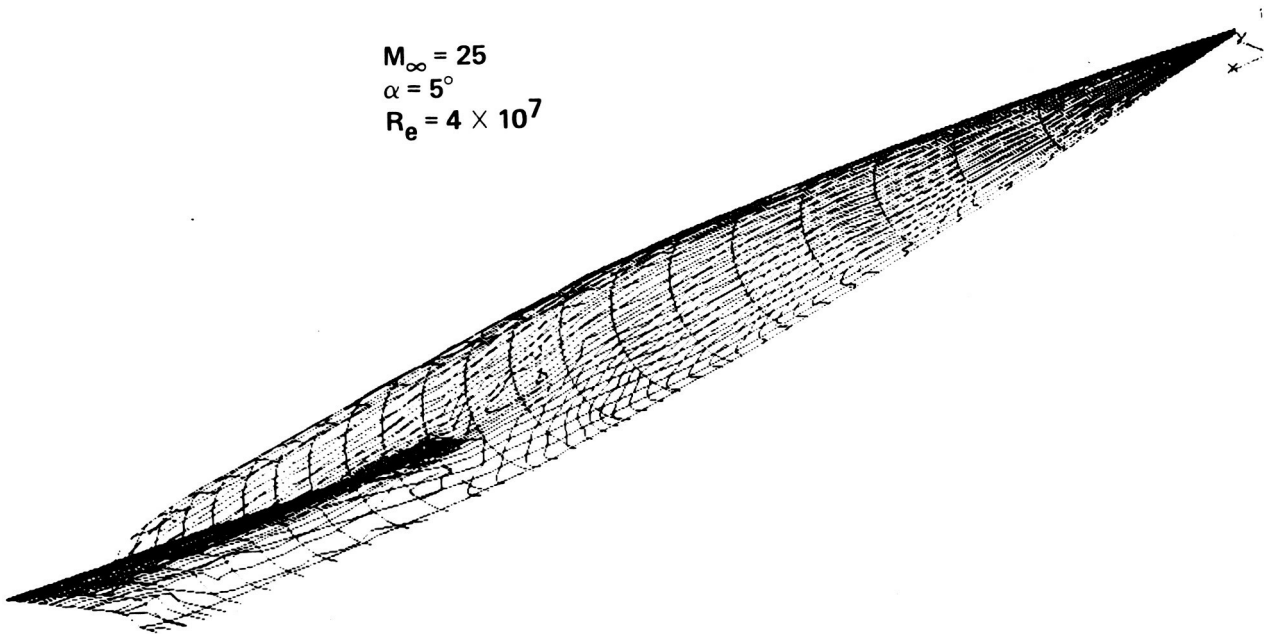


Figure 12. Pressure contours on the body surface.

Report Documentation Page

1. Report No. NASA TM 89444		2. Government Accession No.		3. Recipient's Catalog No.	
4. Title and Subtitle Numerical Simulation of the Hypersonic Flow Around Lifting Vehicles				5. Report Date April 1987	
				6. Performing Organization Code	
7. Author(s) Yehia Rizk (Sterling Federal Systems, Inc., Palo Alto, CA), Denny Chaussee, and Joseph Steger				8. Performing Organization Report No. A-87153	
				10. Work Unit No. 505-61-81	
9. Performing Organization Name and Address Ames Research Center Moffett Field, CA 94035				11. Contract or Grant No.	
				13. Type of Report and Period Covered Technical Memorandum	
12. Sponsoring Agency Name and Address National Aeronautics and Space Administration Washington, DC 20546				14. Sponsoring Agency Code	
15. Supplementary Notes Point of Contact: Yehia Rizk, M/S 258-1, Ames Research Center Moffett Field, CA 94035 (415) 694-4466 or FTS 464-4466 Paper presented at the AGARD symposium on Aerodynamics of Hypersonic Lifting Vehicles, Bristol, UK, April 6-9, 1987.					
16. Abstract A method for solving the viscous hypersonic flow field around realistic configurations is presented. The numerical procedure for generating the required finite difference grid and the two-factored implicit flow solver are described. Results are presented for the shuttle orbiter and a generic wing-body configuration at hypersonic Mach numbers.					
17. Key Words (Suggested by Author(s)) Hypersonic Grid generation Flux splitting				18. Distribution Statement Unclassified-Unlimited Subject Category - 34	
19. Security Classif. (of this report) Unclassified		20. Security Classif. (of this page) Unclassified		21. No. of pages 28	
				22. Price A03	